Hensman, P. J. *et al*. (2024). *Géotechnique* **74**, No. 13, 1765–1779 [https://doi.org/10.1680/jgeot.22.00311]

Monitoring the construction of a deep energy-from-waste bunker in soft clay and peat

PETER J. HENSMAN*†, ZHANDOS Y. ORAZALIN* and BRIAN B. SHEIL‡

This paper describes the monitoring of the construction of a deep underground waste storage bunker for the PROTOS energy-from-waste facility in Chester, UK. A key element of the construction process was a 12 m deep excavation in soft clays and peats which was supported by a complex 'combi-wall' cofferdam comprising alternate tube and sheet piles, a reinforced concrete (RC) capping beam and two levels of internal bracing. The permanent bunker RC structure was constructed within the excavation using a bottom-up approach. The primary aim of this monitoring programme was to assess the performance of the composite support system through measured cofferdam wall deflections, bracing member loads, and site and bunker water levels. An additional objective of the monitoring was to provide the site team with real-time feedback to inform the construction process. Interpretation of the monitored data allows for a quantitative assessment of the influence of various construction activities on the responses of the support system. The monitored behaviour shows that the high stiffness and embedment depth of the supporting structure, combined with careful control of groundwater levels, significantly reduced risks associated with deep excavation construction in challenging ground conditions.

KEYWORDS: excavation; field instrumentation; monitoring; sheet piles & cofferdams

INTRODUCTION

Rapid population growth in dense urban environments means that exploitation of underground spaces is often the only sustainable solution for the delivery of new infrastructure. Driven steel cofferdams are one of the most popular earth-retaining solutions for underground construction. Understanding the performance of a cofferdam structure, and its interaction with the soil, is critical to ensure safe and efficient construction. Robust and reliable construction monitoring is highly desirable to (*a*) verify and refine empirical design approaches (Clough & O'Rourke, 1990; Long, 2001; Moormann, 2004) and (*b*) provide live feedback to site personnel to reduce construction risks and optimise site activities.

The monitored performance of diaphragm and secant pile retaining walls has been a popular topic in the geotechnical literature and dominates deep excavation case histories – for example, Ou *et al*. (1993), Finno *et al*. (2002), Hewitt *et al*. (2003), Finno & Roboski (2005), Liu *et al*. (2005), Liu *et al*. (2011), Ng *et al*. (2012), Tan & Wei (2012), Wu *et al*. (2013), Finno *et al*. (2015) and Cheng *et al*. (2021). Individual case histories are valuable for their site-specific construction challenges, such as the complex excavation work for the construction of the Massachusetts Institute of Technology campus (Orazalin *et al*., 2015) and deep excavations in the historical centre of Rome (Masini *et al*., 2021). These studies also offer opportunities to collate results across many sites to achieve new insights and update design methods – for example, Peck (1969), Mana & Clough (1981) and Wang *et al*. (2010). Although the use of sheet pile retaining walls has been shown to lead to larger maximum wall displacements compared to diaphragm and secant pile walls, reported case histories are relatively scant (Long, 2001; Moormann, 2004). While recent research has significantly advanced understanding, insights are specific to Chicago (Finno *et al*., 1988, 1989, 2019; Finno & Roboski, 2005) and Gothenburg soft clays (Johansson & Sandeman, 2014; Langford *et al*., 2021; Tornborg *et al*., 2021).

Modern cofferdam installation techniques have also led to an increase in the use of 'combi-wall' cofferdam solutions, involving sheet piles interspersed with stiffer king (often tubular) piles, to increase lateral stiffness and bearing capacity. High-quality field data for this support system are much less common; for example, 16 of the 296 case studies reported in Long (2001) related to a combi-wall design, and only one involved a tube and sheet pile combination. There is also a general lack of reported case histories specific to the UK, which have been limited to diaphragm and secant pile walls in London Clay – for example, St John *et al*. (1992), Carder (1995) and Fernie & Sucking (1996). The literature points to a distinct lack of observations on the performance of combi-wall systems in UK soils.

This research gap is addressed in the current paper by describing the monitoring of a 12 m deep excavation supported using a combi-wall solution in soft clays and bands of organic peats in Chester, UK. The support structure was instrumented for the measurement of cofferdam wall deflections, bracing member forces, and site and excavation groundwater levels. Novel aspects of this work include: (*a*) new monitoring data for an unusual combi-wall support system in UK soft soils; (*b*) new insights into the effects of vibratory piling within the excavation on lateral wall displacements and support structure loads; and (*c*) new guidance on end fixity factors for temperature effects on prop loads.

Manuscript received 5 October 2022; revised manuscript accepted 14 June 2023. First published online ahead of print 4 August 2023. Discussion on this paper closes 01 April 2025; for further details see p. ii.

* Department of Engineering Science, University of Oxford, Oxford, UK.
† Ward and Burke Construction Ltd, 25–26 Ivor Place, London, UK.
‡ Formerly University of Oxford, Oxford, UK; now Laing O'Rourke Centre for Construction Engineering and Technology, Department of Engineering, University of Cambridge, Cambridge, UK.

PROJECT DESCRIPTION

Project overview

The construction works described in this paper form part of the PROTOS energy-from-waste project in Chester, UK. The facility is designed to process over 400 000 t of non-recyclable waste per annum to produce up to 49 MW of electrical power. The proposed site is situated on marshland, close to the Manchester ship canal and the River Mersey, as shown in Fig. 1. A key aspect of the project involved the construction of a 40 m long, 18 m wide underground waste storage bunker. Construction of the underground bunker section began with a 12 m deep excavation in May 2021 and was completed in March 2022 by Ward and Burke Construction Ltd.

Ground conditions

The available site investigation included 13 cone penetration tests (CPTs), one of which was a seismic CPT (SCPT), geophysical testing, one borehole, cross-hole seismic testing and laboratory elemental testing. The CPTs and borehole were located around the perimeter of the bunker excavation. The CPTs were performed with a 17·9 t track truck mounted CPT unit (UK20) equipped with a 17·5 t capacity hydraulic ram.

The site investigation results and the inferred stratigraphy are shown in Fig. 2. A 1 m thick layer of made ground (MG) overlies tidal flat deposits (TF), which extend to 12 m below ground level (BGL). The TF deposits are predominantly very low-strength silty clay with two bands of low-strength fibrous peat (P) at 1·0–1·8 m and 9·6–10·3 m BGL. Below ~12 m, there is a ~7 m thick layer of glacial outwash (GO) deposits, which consist of medium dense sands with some gravels. Beneath the outwash deposits lies glacial till (GT) consisting of a 4 m thick layer of stiff, sandy clay (C) with localised silt bands, followed by dense, silty, fine sand containing bands of sandy clay.

The measured pore water pressure, u, closely matches the estimated hydrostatic pore pressure profile, particularly in the coarse-grained soils. From 0–10 m BGL, measurements exceed the hydrostatic calculation, indicating the presence of normally to lightly overconsolidated clays. In contrast, measurements between 20 and 25 m BGL are indicative of moderately to highly overconsolidated materials.

The undrained shear strength, s_u, was determined using the relationship

$$s_u = \frac{q_t - \sigma_{v0}}{N_{kt}} \tag{1}$$

where N_{kt} is the empirical cone factor. A value of $N_{kt} = 20$ was determined by fitting results from 14 unconsolidated, undrained (UU) triaxial compression tests. This value is in good agreement with those calibrated for other UK soft soils in Highbridge ($N_{kt} = 19$) (Royston, 2018) and in Hull ($N_{kt} = 20$) (Allievi *et al.*, 2018). The internal angle of friction of the soil, ϕ', was calculated using the empirical relationship in Kulhawy & Mayne (1990).

From the SCPT, the measured shear wave velocity, V_s, is compared to that inferred from the standard CPT measurements using the method in Robertson (2009), which estimates V_s as a function of q_t and the soil behaviour type index, I_c. The measured data are also plotted using a three-interval linear regression (LR) model. The small-strain shear modulus is calculated according to

$$G_0 = \rho V_s^2 \tag{2}$$

where ρ is the soil density.

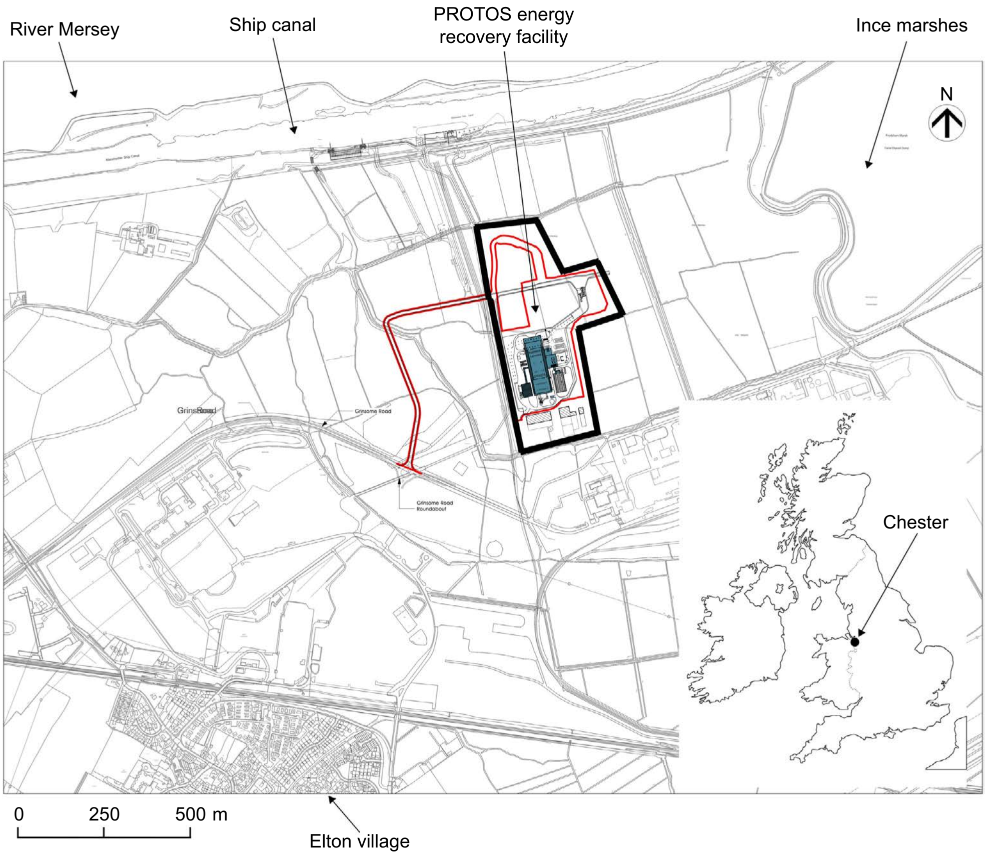

Fig. 1. PROTOS energy-from-waste facility location in Chester, UK. Site boundary shown in black. A full-colour version of this figure can be found on the ICE Virtual Library (www.icevirtuallibrary.com)

Results from a series of laboratory density tests are compared to a depth profile of density inferred from the CPT data using the method in Robertson (2010). The index data are plotted on a combined linear–log scale to highlight the considerable variability observed in the TF layer, which is indicative of the presence of bands of organic peat. Density and index tests performed on samples taken from the lower clay layer suggest a higher degree of uniformity, with density and plasticity remaining approximately constant.

The site water level was measured to vary between 0 and 0·75 m BGL using four piezometers installed to a depth of 15 m; this was likely to be due to the proximity of the excavation to the River Mersey estuary.

Construction sequence

The construction timeline is broken into 17 different construction stages, as summarised in Table 1; schematic illustrations of four of the key stages during construction are shown using sections through the bunker in Fig. 3. Prior to cofferdam installation, precast concrete piles were driven around the bunker area, to act as foundations for adjacent RC building slabs. A driven steel temporary works cofferdam was chosen for excavation support instead of in situ concrete owing to concerns over potential losses of cement fines in the weak clay and peat layers. To minimise ground movements, a combi-wall, comprising alternate tube and sheet piles, was used. The piles were driven to a depth of 21 m into the GT clay layer to minimise seepage into the excavation, with

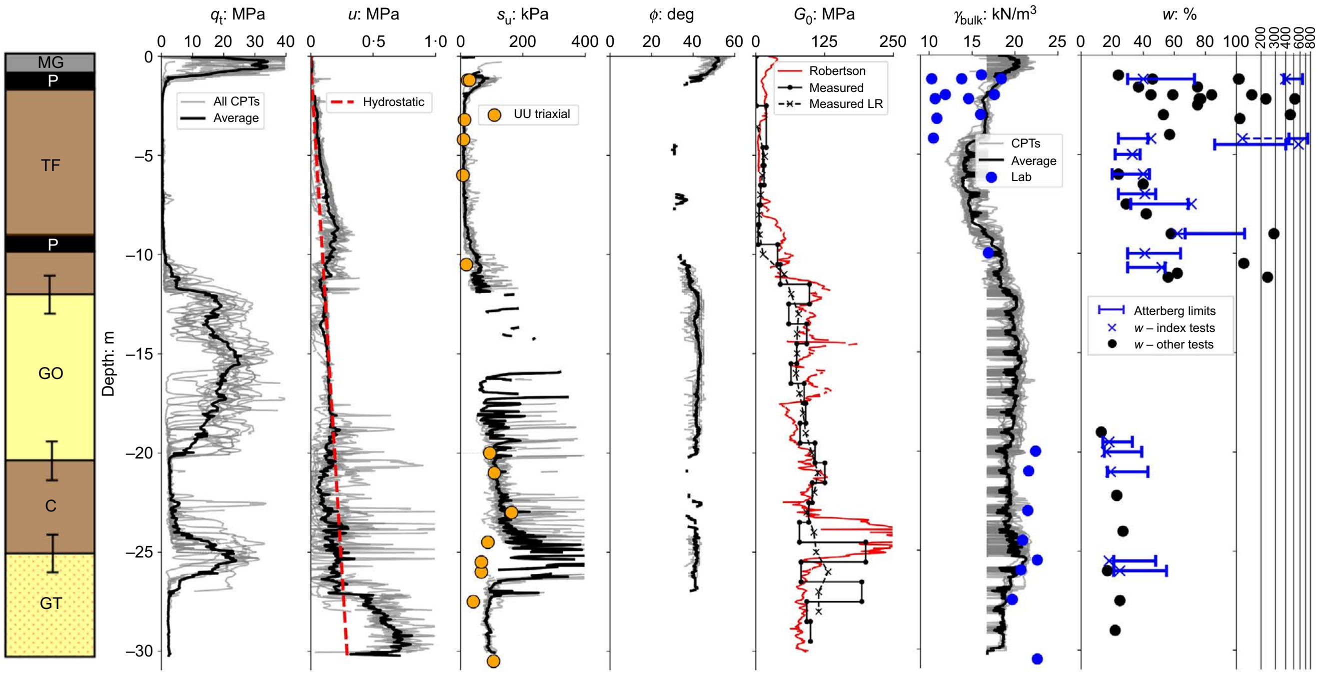

Fig. 2. Measured and inferred soil properties from the CPTs, SCPT and laboratory testing performed around the bunker excavation at PROTOS together with the best estimate of the soil stratigraphy. Grey lines indicate individual CPTs whereas black lines denote the mean of all CPTs (MG, made ground; TF, tidal flat deposits; P, peat; GO, glacial outwash; C, clay; GT, glacial till)

Table 1. Summary of construction sequence

Construction works	Stage	Activity	Start date	End date	Duration: days
Bunker excavation	1	Central frame assembly	11 May 2021	18 May 2021	7
	2	Cofferdam installation	18 May 2021	9 June 2021	22
	3	Excavate tube piles and concrete	14 June 2021	17 June 2021	3
	4	Initial excavation below frame	17 June 2021	20 June 2021	3
	5	Capping beam construction	18 June 2021	09 Aug. 2021	52
	6	Dewatering well installation	9 Aug. 2021	23 Aug. 2021	14
	7	Top prop installation	15 Aug. 2021	31 Aug. 2021	16
	8	Excavation phase 1	1 Sept. 2021	10 Sept. 2021	9
	9	Central frame positioning	10 Sept. 2021	21 Sept. 2021	11
	10	Excavation phase 2	21 Sept. 2021	29 Sept. 2021	8
Bunker piling	11	Piling bunker foundation slab	8 Oct. 2021	2 Nov. 2021	25
Bunker construction	12	Bunker base construction	2 Nov. 2021	25 Nov. 2021	23
	13	Central frame removal	29 Nov. 2021	6 Dec. 2021	7
	14	Bunker wall pour 1 construction	6 Dec. 2021	20 Dec. 2021	14
	15	Bunker wall pour 2 construction	6 Jan. 2022	24 Jan. 2022	18
	16	Top prop removal	31 Jan. 2022	3 Feb. 2022	4
	17	Bunker wall pour 3 construction	3 Feb. 2022	25 Feb. 2022	22
		Underground waste bunker construction	**11 May 2021**	**25 Feb. 2022**	**290**

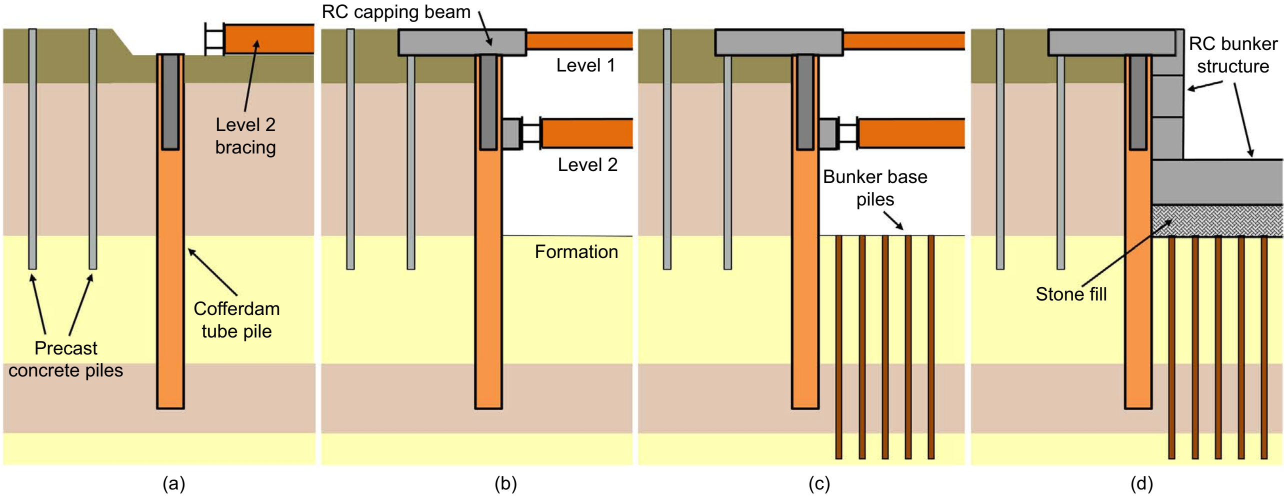

Fig. 3. Typical section through excavation wall at key stages of the construction sequence: (a) stage 3; (b) stage 10; (c) stage 11; (d) stage 17

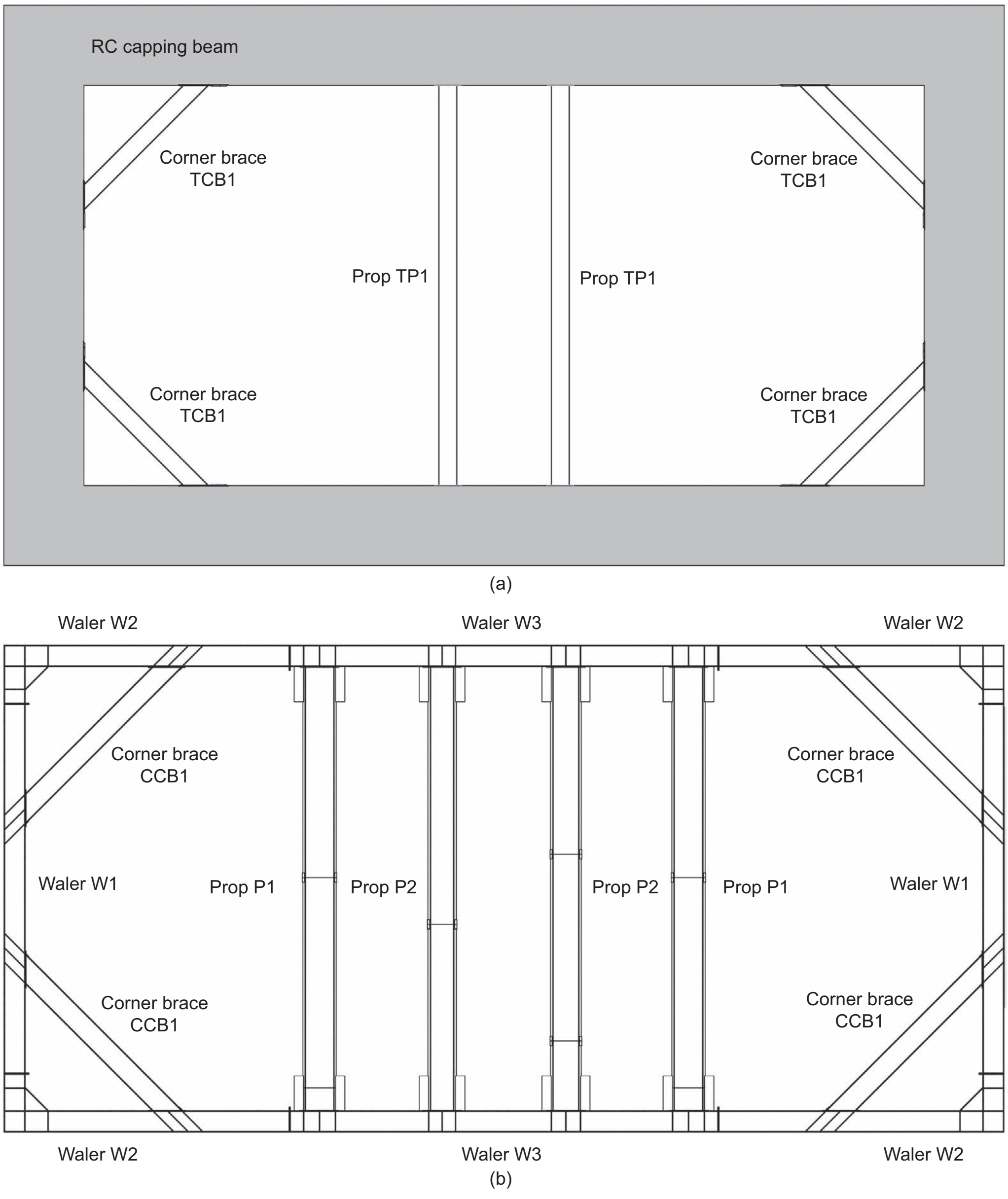

Fig. 4. Schematic illustration of the plan view of the bracing arrangement and member labels for (a) level 1 (top) and (b) level 2 (lower)

AZ28 sheet pile pairs subsequently driven between each tube (stage 2). The tube piles were then internally augered to 6·3 m BGL and filled with concrete to prevent local buckling at frame level 2, as shown in Fig. 3(a) (stage 3).

A 1·2 m thick RC capping beam was constructed around the perimeter of the cofferdam (stage 5), connected to the cofferdam using UC members partially cast into each tube. The cofferdam was supported by two sets of internal bracing at the levels shown in Fig. 3(b); a plan view of the top level 1 bracing (0·6 m BGL) and lower level 2 bracing (5·75 m BGL) is shown in Figs 4(a) and 4(b), respectively. Table 2 presents key properties of each structural member of the cofferdam and support structures.

Dewatering was carried out using internal wells, installed to a depth of 25 m BGL (stage 6), after which excavation commenced and the upper level 1 bracing was installed (stage 7). Excavation was paused to install the lower level 2 bracing frame at 5·75 m BGL (stage 9) before the second and final excavation phase (to a depth of 12 m BGL), was completed (stage 10). The formation depth ensured that the RC bunker base was founded on the GO silty sand deposits.

Construction of the 2 m thick RC base began by installing 156 13 m long, 350 mm dia. steel tubal piles (stage 11), driven vertically from formation depth over the plan area of the excavation (see Fig. 3(c)). The level 2 bracing structure was subsequently removed (stage 12/13) before the bottom-up (BU) construction of the 1·5 m thick RC bunker walls using a one-sided hydraulic climbing formwork structure. Each wall pour had a height of 3 m, with three wall pours required to complete the underground section of the bunker. The level 1 bracing was removed following the second wall pour.

Photographs of the excavation at six different construction stages are presented in Fig. 5.

Table 2. Member properties for steel excavation components

Member type	Label	Section geometry	Length: m	Cross-sectional area, A: cm^2	Elastic modulus, Z: cm^3
Perimeter waler	W1	Double 914/419/343 UB	15·84	874	27 452
	W2	Double 914/419/343 UB	12·23, 2·50*	874	27 452
	W3	Double 914/419/343 UB	18·36	874	27 452
Corner brace	CCB1	Double 914/419/343 UB	6·67	874	27 452
	TCB1	Double 914/419/343 UB	6·90	874	27 452
Central tube	P1	Tube: OD = 1425 mm, t = 22 mm	19·02	970	33 495
	P2	Tube: OD = 1220 mm, t = 20 mm	19·02	754	22 255
	TP1	Tube: OD = 914 mm, t = 20 mm	19·94	562	12 286
Cofferdam	—	Tube: OD = 1220 mm, t = 22 mm, AZ28 sheet pile pairs	21·00	—	9513†

Note: OD denotes external diameter.
*L-shaped waler, length of each section provided.
†Combined tube and sheet pile Z.

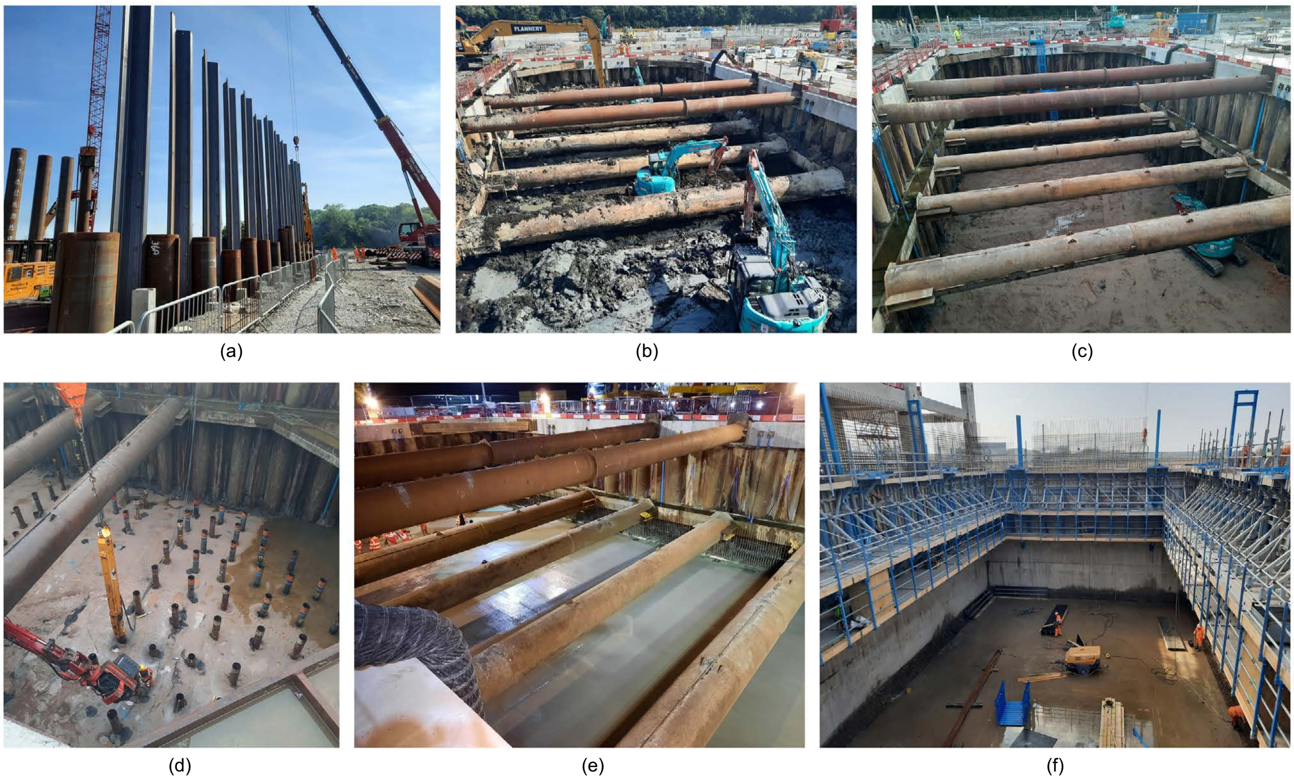

Fig. 5. Photographs of the excavation and bunker structure during construction: (a) stage 2; (b) stage 8; (c) stage 10; (d) stage 11; (e) stage 12; (f) stage 17

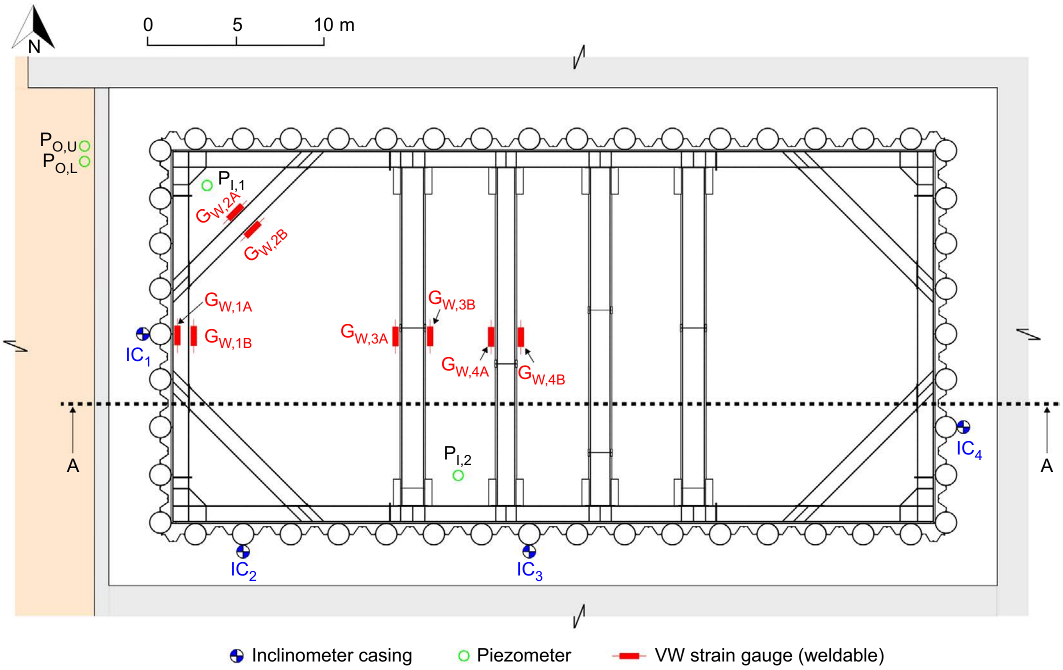

Fig. 6. Plan layout of instrumentation used during excavation, taken through level 2 bracing

FIELD INSTRUMENTATION

The adopted instrumentation set-up for the excavation and bunker construction processes are shown in Fig. 6 and are summarised in Table 3 along with their notation. The information obtained included cofferdam pile deflections, prop member axial loads and bending moments, and water level monitoring data. Video monitoring was undertaken using time-lapse cameras positioned around the site and drones, operating once a week. All data were displayed in real time on a bespoke online platform, accessible to site personnel by way of tablets. The monitored data were continuously compared to trigger early warning and work stoppage thresholds determined from the excavation design calculations. The performance of the support system was evaluated through comparisons to the excavation design and to published empirical guidelines and limits.

Inclinometers

The lateral deflection of the cofferdam was monitored using a portable micro-electromechanical system inclinometer, in casings installed on four of the tube piles (IC_1–IC_4) as shown in Fig. 6. Each 15 m long casing was installed in a bespoke void formed by stitch welding a 100 mm square hollow section length with a tapered base to the tube piles before installation. Each casing was held within the void using a single size 1 mm filter sand. Measurements were taken in an axis both parallel and perpendicular to the cofferdam wall, at 0·5 m intervals starting from the bottom of the casing.

Weldable VW strain gauges

Only the loads in the level 2 bracing were monitored, as this level was considered the priority due to the more significant design loading. To obtain the axial loads and bending moments in the level 2 frame structure, two vibrating wire (VW) strain gauges were tack welded on opposite sides of each of the four instrumented members, as shown in Fig. 6. Measurements were transmitted to a central gateway located at the site office by wireless nodes in the excavation, at a period of 5 min. The average axial prop load, *F*, and bending moment, *M*, were calculated as

Table 3. Bunker instrumentation summary

Measurement	Sensor type	Quantity	Notation
Horizontal wall deflections	Portable inclinometer	4	IC
Prop axial loads and bending moments	Weldable vibrating wire (VW) strain gauge	8	G_W
Water levels – inside and outside of bunker	Piezometer	4	P

$$F = \frac{(\mu\varepsilon_A + \mu\varepsilon_B)}{2} EA \tag{3}$$

$$M = \frac{(\mu\varepsilon_A - \mu\varepsilon_B)}{2} EZ \tag{4}$$

where *Z*, *E* and *A* are the elastic modulus, Young's modulus (taken as 210 GPa for steel) and cross-sectional area of the member considered, respectively, and $\mu\varepsilon_A$ and $\mu\varepsilon_B$ denote the microstrain measurement on either side of a given member.

Piezometers

Two inner piezometers ($P_{I,1}$, $P_{I,2}$) and two outer piezometers ($P_{O,U}$, $P_{O,L}$) were installed to monitor internal and external bunker water levels, respectively. A section showing the installation level of each of the monitoring wells is shown in Fig. 7. The external boreholes were positioned to

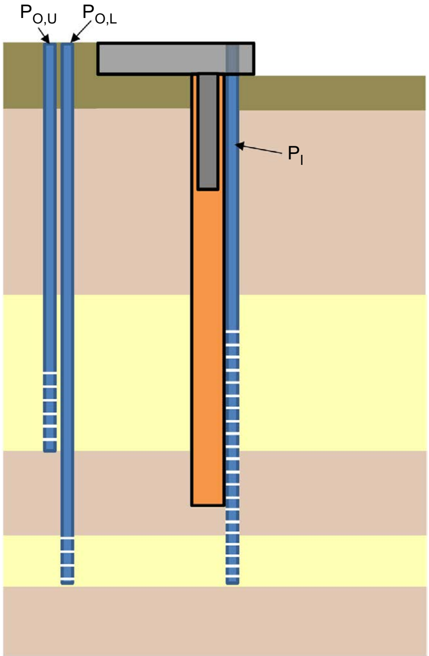

Fig. 7. Section through excavation showing piezometer installation levels. Perforated pipe lengths are indicated by the dashed lines. Plan locations are given in Fig. 6

determine whether groundwater was being drawn into the excavation by the internal pumps, and whether the GT clay layer achieved an effective seal between the GO and GT sand below.

OBSERVED COFFERDAM DEFLECTIONS

Maximum deflection–time history

A time history of the maximum lateral displacement, $\delta_{h,max}$, experienced by the four monitored tubes (IC_1–IC_4) is presented in Fig. 8. For reference, the average surveyed excavation level is plotted using a secondary axis and key construction activities are indicated using shaded regions. The development trends of $\delta_{h,max}$ for all four monitored tubes during construction are similar. The largest $\delta_{h,max}$ (= 23·2 mm) during excavation was recorded for IC_1, which was 1·4–1·7 times greater than those recorded for IC_2–IC_4 due to its position at the centre of the west wall and the presence of a plant access road, and therefore additional surcharging, on the west side. It is also likely that IC_2 and IC_4 experienced beneficial 'corner effects' (Roboski, 2004). A significant increase is observed for IC_3 during the bunker piling, indicating a much greater effect of this activity on the long span of the support system. Negligible changes are observed following base construction.

Deflected shape during excavation

All tube piles around the perimeter of the cofferdam were surveyed before and after the initial 1·5 m deep excavation (stage 4 in Table 1) to monitor lateral deflection at the cantilever stage. The average ratio of cantilever deflection to maximum deflection for the four monitored tube piles $\delta_{h,c}/\delta_{h,max} = 1{\cdot}19$ is significantly larger than the range of 0·3–0·6 reported in Gaba *et al*. (2017) for excavations in London Clay, indicating that the passive resistance provided by the soft TF layers following removal of the stiffer MG band is much less than that provided by the stiffer London Clay.

Figure 9 shows the horizontal displacement, δ_h, profiles with depth measured for IC_1–IC_4 at several stages during excavation together with (long-span) cross-sections of the corresponding excavation surface profile. It can be seen that the RC capping beam was highly effective at 'anchoring' the top of the cofferdam. Interestingly, negative lateral displacements initially develop at ~1·5 m BGL for IC_4 due to shallow excavation works (to a depth of ~1 m) occurring behind the capping beam during the construction of a RC slab. As excavation depth, H, increases, there is a steady increase in both $\delta_{h,max}$ and its corresponding depth, to the point where $\delta_{h,max}$ occurs near the dig level at the end of excavation. The largest percentage increases in $\delta_{h,max}$ caused by excavation phase two were 210% and 136% for IC_3 and IC_4, respectively, on the east side of the bunker, whereas 82% and 95% increases were observed for IC_1 and IC_2, respectively. This may be attributed to the additional 0·5 m depth excavated on the east side, compared to the west side during this period.

Deflected shape during bunker construction (post-excavation)

Figure 10 shows the profiles of δ_h with depth during bunker piling, which is broken into four different 'piling weeks' (WK1–WK4), as shown in the pile installation layout in Fig. 10(b). Bunker piling causes substantial increases in δ_h for all four monitored tube piles. In contrast, no appreciable changes to the corresponding depths to $\delta_{h,max}$ or the overall deflected shapes are observed. Measured displacements are strongly influenced by nearest proximity piling, whereas other piling has only a secondary effect. For example, WK1 piling causes a significant increase in IC_4 displacements, which then show negligible changes during subsequent piling. In contrast, there is a steady increase in $\delta_{h,max}$ for IC_2 and IC_1 during this period as the piling progressed towards the west side of the bunker. The piling process had the greatest impact on the long-span IC_3 measurements with an increase in $\delta_{h,max}$ of 111%, which is likely to be due to its closer proximity to the bunker piles.

Following piling, the 2 m thick RC base is cast with all temporary propping still in place. From Fig. 10(a), base installation causes a small decrease in $\delta_{h,max}$ for IC_1 and IC_3 and a small increase in $\delta_{h,max}$ for IC_2 and IC_4. This suggests a competing influence of the outward concrete head and the subsequent concrete shrinkage during curing.

Comparison to previous case histories and empirical design methods

The maximum wall displacement and its corresponding depth BGL ($z[\delta_{h,max}]$) are plotted as a function of the final excavation depth in Figs 11(a) and 11(b), respectively. Empirical relationships and data from previous case histories are also superimposed on these plots for comparison. The adopted selection of empirical design rules represents a mix of average expected displacements and recommended upper limits for design, and are defined in Table 4. From Fig. 11(a), present measurements span a relatively broad range. Fernie & Sucking (1996) (labelled [4] in the figure) recommended that an average of $\delta_{h,max}/H = 0{\cdot}15\%$ provides a reasonable fit to the data during the excavation process, whereas the upper limit of $\delta_{h,max}/H = 0{\cdot}5\%$ (Clough & O'Rourke, 1990) represents a safe design bound for the present data. Bunker piling and construction causes the displacements to increase above several average and bound lines at the end of construction, thus highlighting the importance of considering all stages of construction in design.

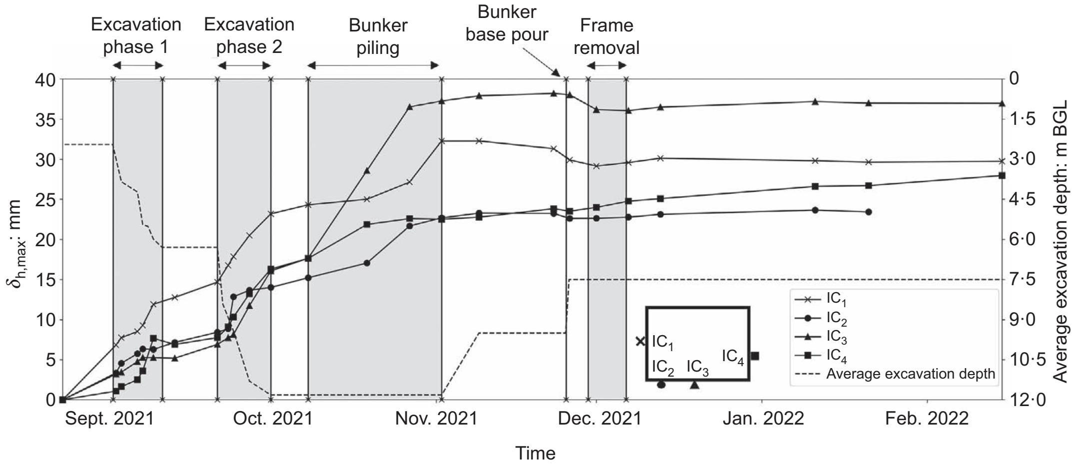

Fig. 8. Time history of instrumented tube pile maximum lateral displacements and average internal level

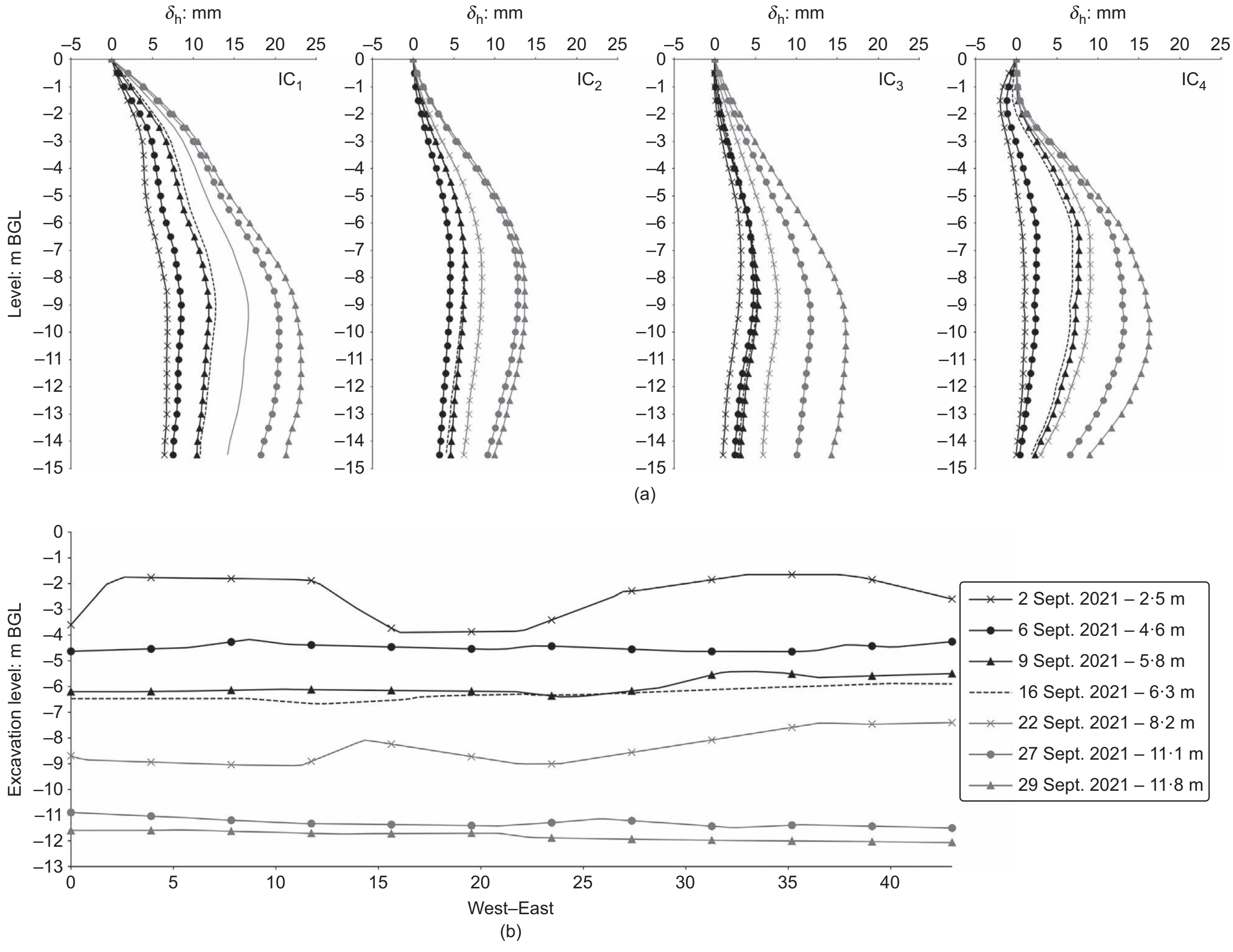

Fig. 9. (a) Horizontal displacement profiles for instrumented tube piles during bunker excavation. (b) Corresponding bunker excavation level surveys taken through section A–A in Fig. 6, and legend. Phase 1 excavation and phase 2 excavation indicated by black and grey lines, respectively

In Fig. 11(b), the present monitored data are compared with those reported by Moormann (2004) in layered soils representing either soldier or sheet pile walls (denoted 'SS') or contiguous, secant pile and diaphragm walls (denoted 'CSD'). The present measurements are well described by the $z[\delta_{h,\max}]/H = 1{\cdot}0$ guideline (Moormann, 2004), indicating that the point of maximum displacement is approximately located at the dig level during excavation. This is consistent with the reported behaviour of walls supporting soft clays in China, with maximum lateral wall deflections in stiff clays typically occurring further above the excavation level (Tan *et al.*, 2018), highlighting the soft nature of the TF layers.

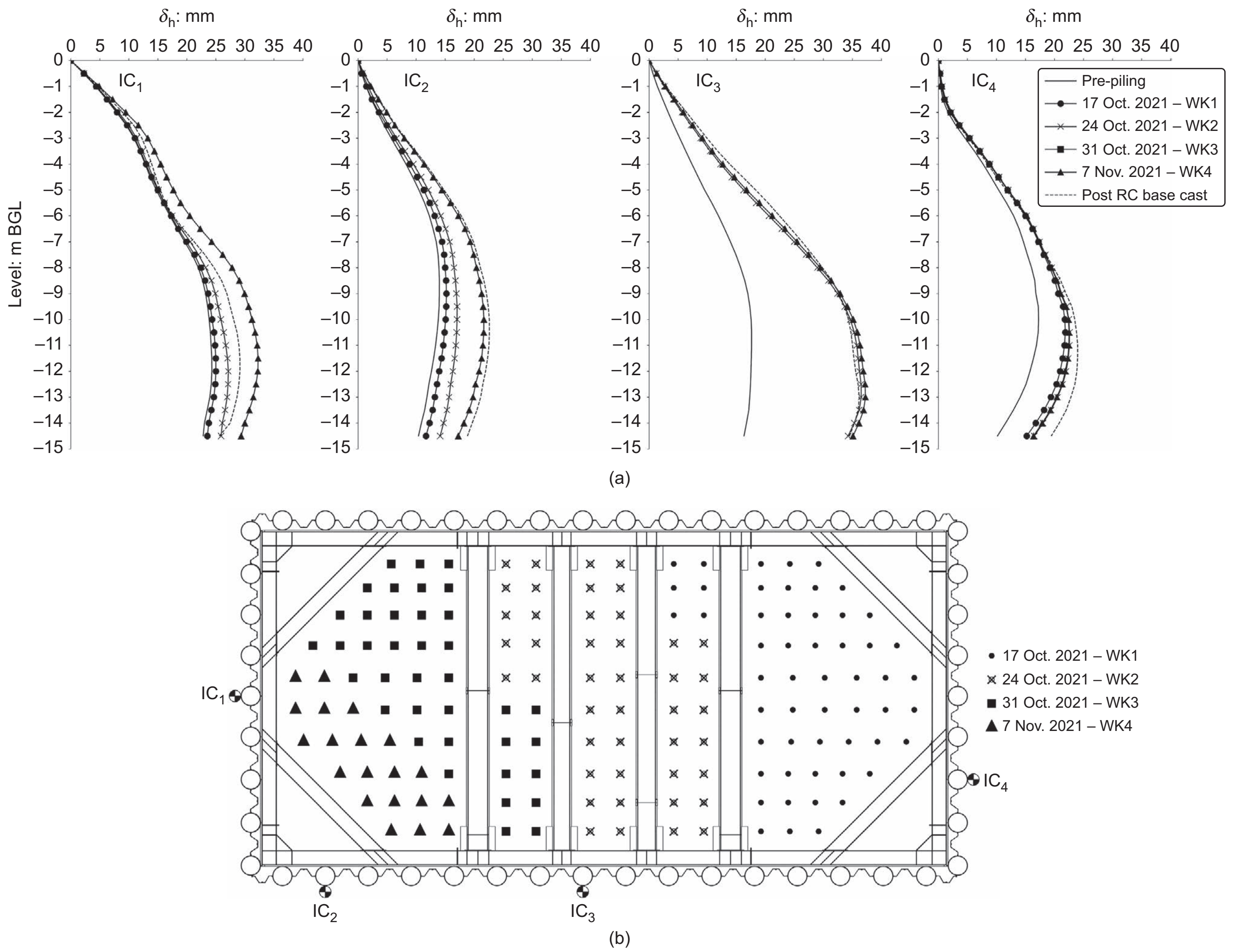

Fig. 10. (a) Measured δ_h profiles with depth for all four instrumented tube piles during internal piling works and RC bunker base construction (WK3 profiles omitted due to sensor fault); (b) corresponding weekly pile installation layout

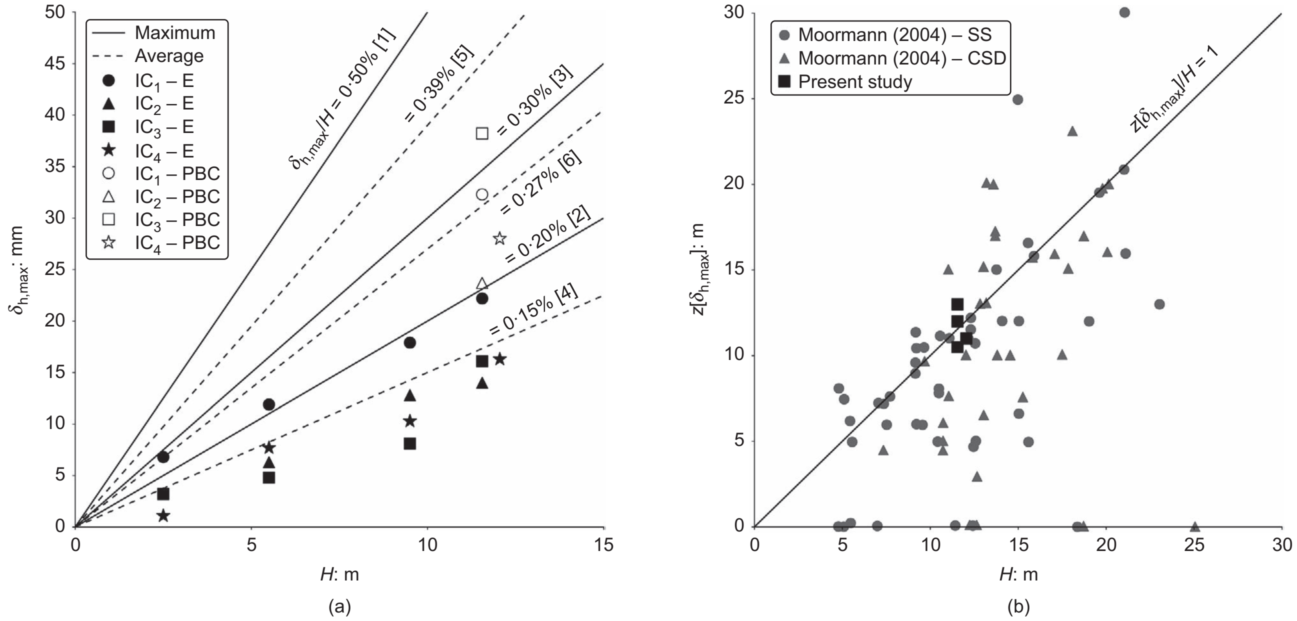

Fig. 11. Comparison between present monitored data and empiricism reported elsewhere in the literature: (a) variation of $\delta_{h,max}$ with H both during excavation (denoted by E) and post bunker construction (denoted by PBC) (refer to Table 4 for empirical design rule definition and notation [1]–[6]); (b) variation of $z[\delta_{h,max}]$ with H. SS denotes sheet and soldier pile walls, CSD denotes contiguous, secant pile and diaphragm walls

Table 4. Empirical $\delta_{h,max}/H$ ratios reported in the literature

Reference	Support system type	Design rule notation	$\delta_{h,max}/H$: %	Description	Soil conditions
Clough & O'Rourke (1990)	SS, CSD	[1]	0·5	Maximum	Soft clays
		[2]	0·2	Maximum	Stiff clays
Fernie & Sucking (1996)	CSD	[3]	0·3	Maximum	Stiff London Clay
		[4]	0·15	Average	
Long (2001)	SS, CSD	[5]	0·39	Average	Retaining soft soils, embedded in stiff soils ('case 2')
Moormann (2004)	SS, CSD	[6]	0·27	Average	Layered soils

Note: SS denotes sheet and soldier pile walls, CSD denotes contiguous, secant pile and diaphragm walls.

OBSERVED PROP AXIAL LOADS AND BENDING MOMENTS

A time history of the overall axial and bending loads for each instrumented level 2 bracing member is shown in Figs 12(a) and 12(b), respectively; key construction stages are again identified using grey shading. The measured axial loads show similar trends for all four bracing members. The largest measured axial load is experienced by the corner brace on account of this member being at an angle to the cofferdam wall and having the largest tributary area (and vice versa for the perimeter waler). Predictably, there is a noticeable increase in axial loads during the excavation phase, due to stress redistribution from the internal soil to the support structure.

Significant increases in axial loads are also caused by the vibratory piling. While WK1 and WK2 piling had little influence on the axial loads, significant increases occurred during WK3 and WK4 as piling progressed towards the instrumented members on the west side of the bunker (see Fig. 10(b)). These considerable load increases and the associated increases in lateral wall deflection in Fig. 10 are due to a loss of strength of glacial till clay (C) inside the excavation consequent upon remoulding and excess pore pressure generation caused by pile driving. The vibratory piling may have also induced liquefaction effects in the saturated GO layer. These results highlight the importance of considering the impact of the full construction process on the adopted support system.

Following the casting of the RC bunker base, a significant reduction in compressive axial load of 91%, 41%, 29% and 36% was observed for W1, CCB1, P1 and P2, respectively. This can be attributed to a redistribution of the bracing forces into the RC base, which undergoes thermal expansion during cement hydration. This behaviour is consistent with the reductions in prop loads of ~10% and ~20% following base slab installation reported in Powrie & Batten (2000) and Chambers *et al*. (2016), respectively. Finally, post-excavation removal of the frame caused notable increases in axial load, as removed frame member loads redistributed into adjacent members.

Similar findings may be deduced from an examination of the bending moments in Fig. 12(b). The largest bending moments developed in the corner brace, which may be attributed to the significant eccentricity of the applied cofferdam load. The two central tube props experience bending towards the west side of the bunker, which suggests the long-span waler on the north side of the bunker is exhibiting curvature towards the excavation, which is symmetric about the centre of the span. The magnitude of the bending moment measured in P1 is significantly larger than that in P2, owing to P2's closer proximity to the centre of symmetry on the north waler.

The maximum distributed prop load per unit tributary area (DPL) is calculated as 195, 152, 140 and 145 kN/m^2 for W1, CCB1, P1 and P2, respectively. Of the values of DPL for over 300 prop members supporting deep excavations reported in Twine & Roscoe (1997), 86% fall below the smallest measured DPL of 140 kN/m^2. This suggests a large proportion of lateral earth loads are transferred into the support structure, highlighting the low strength of the TF layers. The calculated DPL values are consistent with those reported for props supporting excavations in soft clays in Oslo, Norway (NGI, 1962), Chicago, USA (Swatek *et al*., 1972) and Rotterdam, the Netherlands (Tschebotarioff, 1973).

From Fig. 12(a), even though the VW strain gauges were verified to have negligible temperature effects, significant daily fluctuations are observed in the data, due to thermal (expansion) effects experienced by the props. Several methods for compensating for these temperature fluctuations have been reported in the literature (Richards *et al*., 1999; Powrie & Batten, 2000), which involve monitoring temperature fluctuations during downtime periods. By way of an example, Fig. 13 shows the measured microstrain, $\mu\varepsilon$, for gauge $G_{W,3A}$ (multiplied by EA to give an apparent load in kN) plotted against the temperature measured by the gauge thermistor during a downtime period between 1 November 2021 and 20 November 2021. An approximately linear relationship between temperature and measured strain is apparent, indicating strong temperature causation. By calculating the gradient of the assumed linear relationship, f, the prop end fixity factor, FF, can be calculated

$$FF = \frac{f}{EA\alpha} = \frac{f}{f_t} \tag{5}$$

where α is the coefficient of thermal expansion of the prop material, and f_t is the theoretical thermally induced load assuming rigid end restraint. Table 5 summarises the calculation of FF for each of the level 2 frame gauges. There is good consistency between the values of FF for pairs of gauges on each frame member. The largest values of FF were calculated for waler W1, which is to be expected as the ends of this member are welded to those members adjacent. The smallest values of FF were calculated for the tube props P1 and P2, as these members were hung from the perimeter frame with no other method of connection applied to their ends. The proximity of the member to the corner of the excavation also influenced the calculated FF, indicating increased composite support structure stiffness at the excavation corners. This finding is consistent with the monitored lateral wall deflection behaviour. Except for W1, owing to its welded ends, the calculated FF values are reasonably consistent with the 10–25% range recommended in Twine & Roscoe (1997), based on previous sheet pile wall case histories. The current industry-adopted approach for incorporating prop temperature effects into design in Gaba *et al*. (2017) suggests using FF values of 30% and 50% for stiff walls in soft soils and in stiff soils, respectively. However, no

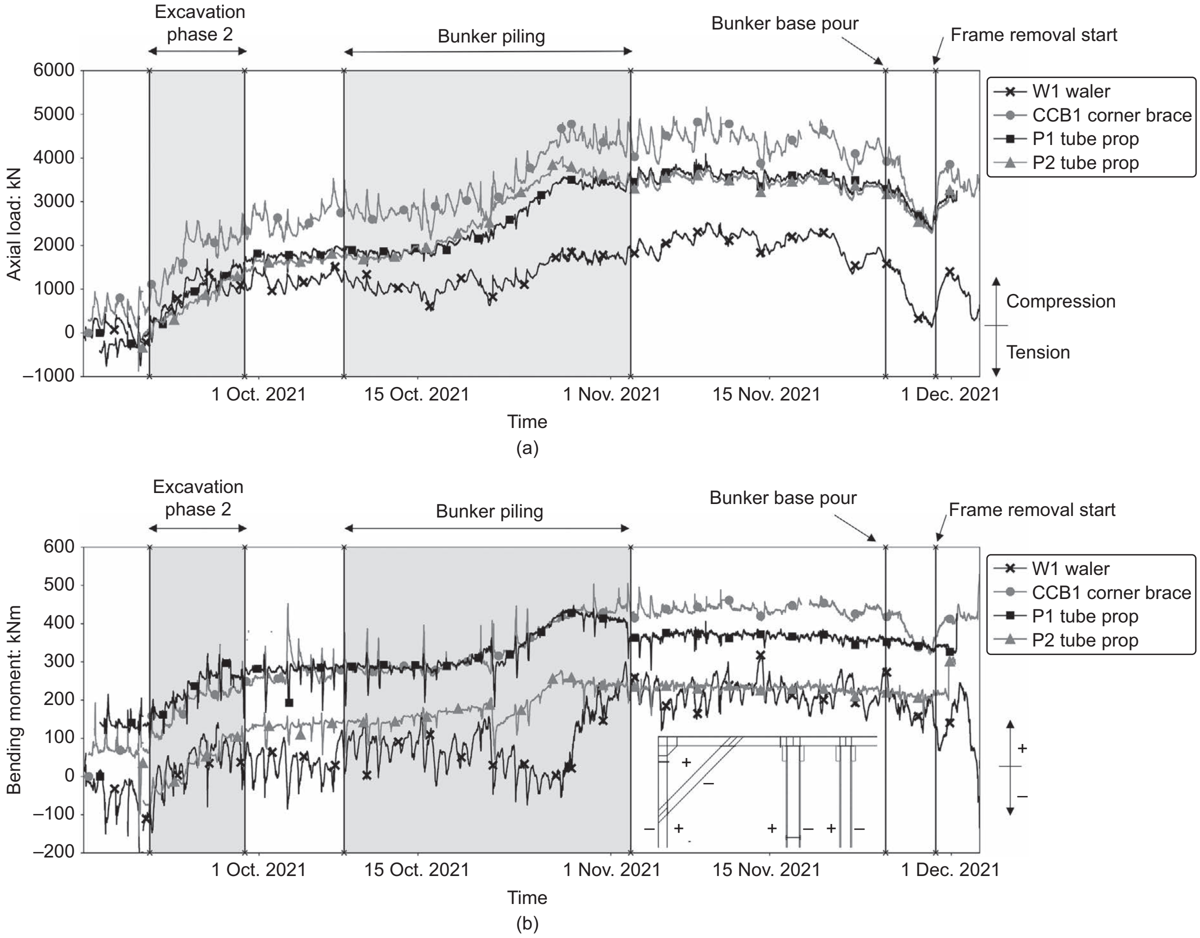

Fig. 12. Level 2 instrumented frame member (a) axial load–time series and (b) bending moment–time series

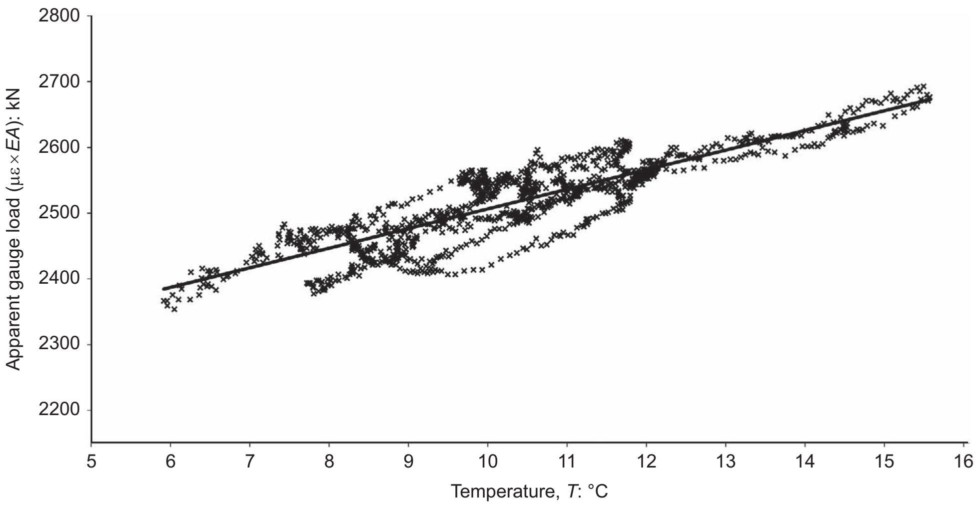

Fig. 13. Typical relationship between temperature and apparent gauge load (gauge $G_{W,3A}$) during a period of no construction activity in the bunker area

guidance is provided for excavations supported by more flexible sheet pile walls and combi-walls. Although data from more cases will be necessary to verify or refine the calculated *FF*, the values from this project can be contributed towards this database to provide initial guidance on the selection of *FF* values for these more flexible wall types.

As the relationship between measured strain and temperature for each gauge is approximately linear, the measured prop loads can be adjusted to account for thermal expansion as follows

$$F_{\text{adjusted}} = F - fT \tag{6}$$

where F_{adjusted} are the loads that would have been recorded in each prop had the construction occurred without variation in temperature. Fig. 14 presents a comparison between F and F_{adjusted} for all four instrumented frame members.

Although daily fluctuations in $F_{adjusted}$ are considerably less than those in F, temperature fluctuations have not been eliminated completely. This is due to seasonal variations in differential temperature across the prop and to the member loads–temperature relationships not being truly linear. The largest difference between F and $F_{adjusted}$ is observed for W1 (61·1%) due to the large FF combined with a period of seasonal cooling from September until December. In contrast, there is little difference between F and $F_{adjusted}$ for props P1 and P2 owing to the reduced FF enabling almost uninhibited thermally induced movement. In contrast, temperature compensation had a negligible influence on bending moments due to compensated gauges cancelling each other out.

Table 5. Summary of the end fixity factor, *FF*, calculation for each level 2 frame member gauge

Level 2 frame member	Gauge	f: kN/°C	f_t: kN/°C	FF: %
W1 waler	$G_{W,1A}$	115·1	247·3	46·5
	$G_{W,1B}$	117·6	247·3	47·5
CCB1 corner brace	$G_{W,2A}$	82·2	290·5	28·3
	$G_{W,2B}$	81·0	290·5	27·9
P1 tube prop	$G_{W,3A}$	29·9	230·1	13·0
	$G_{W,3B}$	30·7	230·1	13·3
P2 tube prop	$G_{W,4A}$	29·5	178·9	16·5
	$G_{W,4B}$	31·5	178·9	17·6

OBSERVED WATER LEVELS

The observed water level time series for all piezometers are shown in Fig. 15. For reference, the corresponding time history of the total pumped flow rate, q, is also plotted on a secondary axis. The site water table outside the excavation ($P_{O,U}$) remained consistently high throughout construction, varying between 2 and 3 m above ordnance datum (AOD), due to the close proximity of the River Mersey. Initially three pumping wells were operational, with an average $q = 5{\cdot}5$ l/s, reducing the water table within the bunker ($P_{I,1}$, $P_{I,2}$) to approximately $-5{\cdot}5$ m AOD. This was still 0·7 m above the estimated formation depth, which led to the mobilisation of a fourth pumping well on 1 September 2021, which increased q to 7 l/s and reduced the level to -7 m AOD. During unexpected shutdowns of the pumping system (reflected by $q = 0$), the water level increased rapidly at a rate of 100 mm/min. To reduce the risk to personnel within the excavation and prevent damage to plant, the capacity of the

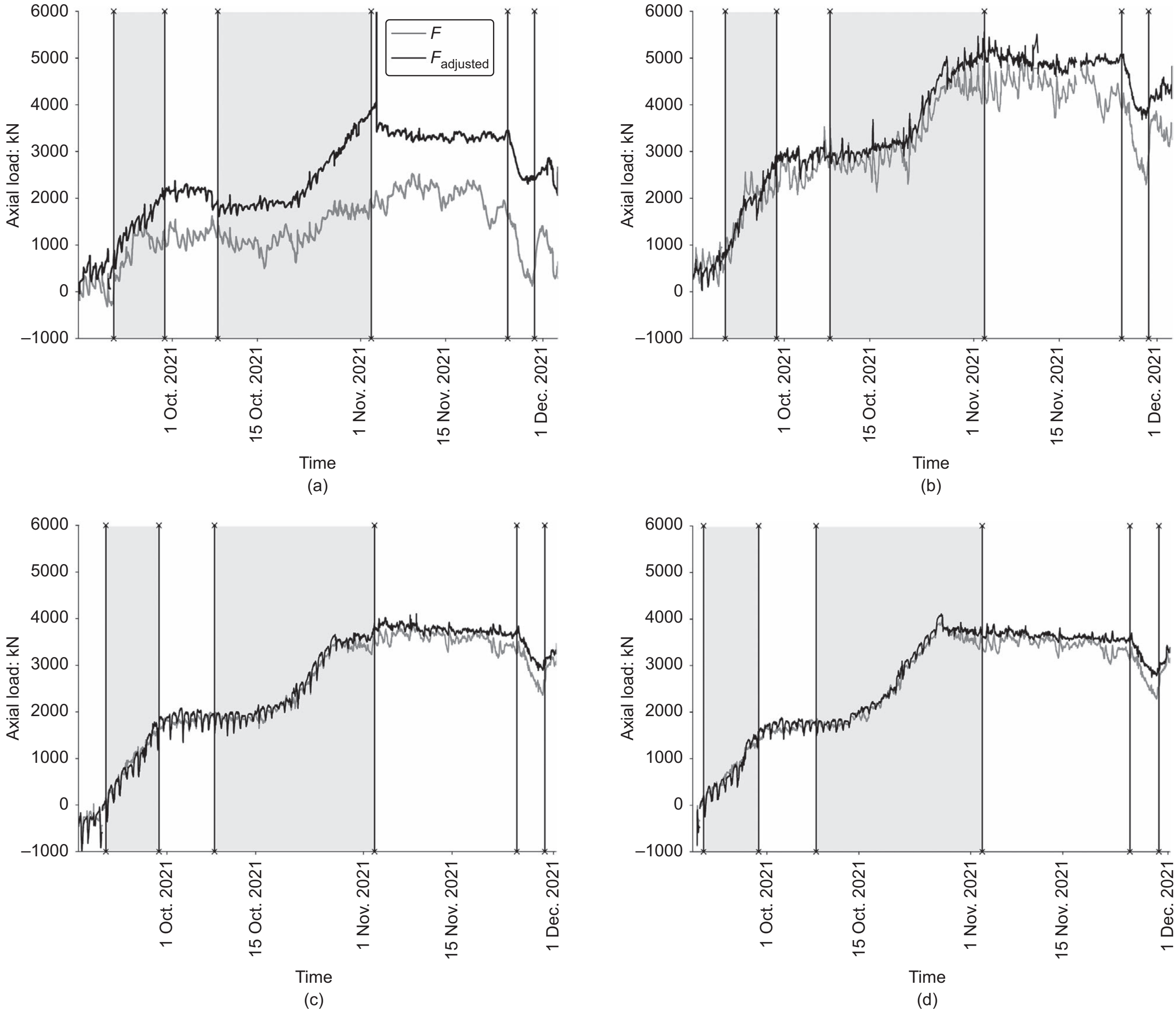

Fig. 14. Comparison between axial load, *F*, and temperature-adjusted axial load, $F_{adjusted}$, for: (a) waler W1; (b) corner brace CCB1; (c) prop P1; (d) prop P2. The construction activities indicated by vertical lines and shaded regions are the same as those annotated in Fig. 12

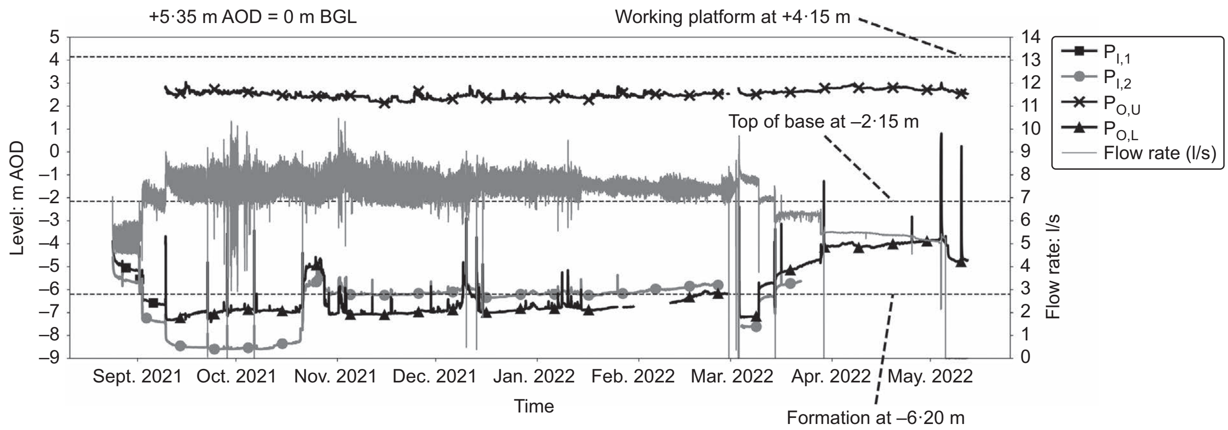

Fig. 15. Piezometer water level data and total pumped well flow rate

pumping system was increased further by repurposing the $P_{I,1}$ monitoring well for a fifth pumping well on 7 September 2021. This reduced the water level to −8·5 m AOD and increased *q* to 8 l/s.

The internal ($P_{I,2}$) and external ($P_{O,L}$) water levels in the lower GT sands show very similar trends except $P_{I,2}$ is consistently ∼1·5 m higher, indicating groundwater is being drawn into the bunker through seepage beneath the cofferdam toe. This behaviour is consistent with that reported in Pujades *et al*. (2014) where seepage occurred beneath the walls of a deep shaft for a high-speed train tunnel in Barcelona, through transmissive layers inside materials of low hydraulic conductivity. During a watertightness testing, the pumped flow rate of 7 l/s achieved a drawdown of ∼10 m, which again is consistent with the measured *q* for this project. This suggests flow through the lower GT layers behaves similarly to that through the Barcelona silty sand layers. The water level in the GO sand layer remains at the site water table level, indicating that the GT clay layer acts as a highly effective seal to prevent flow between the GO and GT granular layers. The mobilisation of bunker piling towards the monitoring well locations (early October 2021) caused an increase in water level of ∼2·2 m in both $P_{I,2}$ and $P_{O,L}$, despite no apparent change in system set-up and a constant $q = 8$ l/s. This reduction in performance may be due to the disturbance and restriction of flow passages in the ground adjacent to the monitoring wells caused by the vibratory piling equipment. The dewatering and water level monitoring schemes directly mitigated and helped manage the risks of flooding, excessive pumping rates and wall infiltration posed by the deep excavation and bunker construction.

CONCLUSIONS

This paper has described the observed performance of a deep excavation retaining soft clays and peats for the purpose of an energy-from-waste facility in the UK. To inform the construction process, a monitoring system was developed to provide real-time feedback to site personnel. The monitoring system enabled the measurement of cofferdam wall horizontal deflections, prop loads, and bunker and site water levels. The main findings of this study can be summarised as follows.

(*a*) Measured wall displacements were well represented by average values reported elsewhere in the literature and were close to lower bounds reported for deep excavations in soft clays; these results highlight the potential applicability of existing solutions and design methods to combi-wall design in soft soils in the UK.

(*b*) Vibratory piling internally within the excavation cause an increase to the horizontal wall displacements of up to 111%, revealing the importance of considering the full construction process on the support system performance.

(*c*) The axial loads measured in the bracing members increased steadily during excavation, with the largest load developed in the corner brace (2300 kN) owing to its relatively large tributary length and it being at an angle to the cofferdam wall. Internal bunker piling caused an increase in member loads of between 700 and 2100 kN.

(*d*) The monitored data showed that temperature-induced axial loads can account for a significant proportion of the total member load for frames installed at low temperatures. The present data reveal a degree of end restraint in the range of 10–30% to be appropriate for deep excavations in soft clays supported by driven steel cofferdams.

(*e*) Continuous groundwater pumping, with flow rates consistently above 7 l/s, was necessary to retain the internal excavation water level below formation level, owing to seepage occurring below the cofferdam toe. Piling within the excavation led to a reduction in the performance of the pumping system due to the introduction of additional flow paths.

DATA AVAILABILITY STATEMENT

Some or all data used in this paper are available from the corresponding author by request.

ACKNOWLEDGEMENTS

The authors gratefully acknowledge the technical guidance and financial support provided by Ward & Burke Construction Ltd for this research, as well as the efforts of the site team at PROTOS energy recovery facility. The authors also thank the team at WJ Groundwater for the installation of the dewatering and water level monitoring systems. This project was supported by the Royal Academy of Engineering under the Research Fellowship Scheme.

NOTATION

A	area
E	Young's modulus
F	axial load
$F_{adjusted}$	temperature adjusted axial load

FF	prop end fixity factor
f	prop temperature gradient
f_t	theoretical thermally induced prop load – rigid end restraint
G_0	small-strain shear stiffness
H	excavation depth
M	bending moment
N_{kt}	cone penetration test cone factor
q	flow rate
q_t	cone penetration test corrected cone tip resistance
s_u	undrained shear strength
T	temperature
t	thickness
u	pore water pressure
V_s	shear wave velocity
w	water content
Z	elastic modulus
$z[\delta_{h,max}]$	depth of position of $\delta_{h,max}$
α	thermal expansion coefficient
γ_{bulk}	soil bulk unit weight
δ_h	lateral displacement
$\delta_{h,max}$	maximum lateral displacement
ρ	soil density
σ_{v0}	in situ vertical stress
Φ	angle of friction

REFERENCES

Allievi, L., Curran, T., Deakin, R. & Tyldsley, C. (2018). On the use of CPT for the geotechnical characterization of a normally consolidated alluvial clay in Hull, UK. In *Cone penetration testing 2018* (eds M. A. Hicks, F. Pisanò and J. Peuchen), pp. 73–78. Leiden, the Netherlands: CRC Press/ Balkema.

Carder, D. R. (1995). *Ground movements caused by different embedded retaining wall construction techniques*, TRL Report 172. Wokingham, UK: Transport Research Laboratory.

Chambers, P., Augarde, C., Reed, S. & Dobbins, A. (2016). Temporary propping at Crossrail Paddington station. *Geotech. Res.* **3**, No. 1, 3–16.

Cheng, K., Xu, R., Ying, H., Gan, X., Zhang, L. & Liu, S. (2021). Observed performance of a 30.2 m deep-large basement excavation in Hangzhou soft clay. *Tunn. Undergr. Space Technol.* **111**, 103872.

Clough, G. W. & O'Rourke, T. D. (1990). Construction induced movements of in situ walls. In *Design and performance of earth retaining structures* (eds P. Lambe and L. Hansen), Geotechnical Special Publication no. 25, pp. 439–470. Reston, VA, USA: American Society of Civil Engineers.

Fernie, R. & Sucking, T. (1996). Simplified approach for estimating lateral wall movement of embedded walls in UK ground. In *Geotechnical aspects of underground construction in soft ground* (eds R. J. Mair and R. N. Taylor), pp. 131–136. Rotterdam, the Netherlands: Balkema.

Finno, R. J. & Roboski, J. F. (2005). Three-dimensional responses of a tied-back excavation through clay. *J. Geotech. Geoenviron. Engng* **131**, No. 3, 273–282.

Finno, R. J., Atmatzidis, D. K. & Nerby, S. M. (1988). Ground response to sheet pile installation in clay. In *International conference on case histories in geotechnical engineering*, pp. 1297–1301. Rolla, MO, USA: Missouri University of Science and Technology.

Finno, R. J., Atmatzidis, D. K. & Perkins, S. B. (1989). Observed performance of a deep excavation in clay. *J. Geotech. Engng* **115**, No. 8, 1045–1064.

Finno, R. J., Bryson, S. & Calvello, M. (2002). Performance of a stiff support system in soft clay. *J. Geotech. Geoenviron. Engng* **128**, No. 8, 660–671.

Finno, R. J., Arboleda-Monsalve, L. G. & Sarabia, F. (2015). Observed performance of the one museum park west excavation. *J. Geotech. Geoenviron. Engng* **141**, No. 1, 04014078.

Finno, R. J., Kim, S., Lewis, J. & Van Winkle, N. (2019). Observed performance of a sheetpile-supported excavation in Chicago clays. *J. Geotech. Geoenviron. Engng* **145**, No. 2, 05018005.

Gaba, A., Hardy, S., Doughty, L., Powrie, W. & Selemetas, D. (2017). *Guidance on embedded retaining wall design*. London, UK: Ciria.

Hewitt, R. D., Haley, M. X. & Kinner, E. B. (2003). Case history of deep excavation on an urban campus. In *Proceedings of the 12th panAmerican conference on soil mechanics and geotechnical engineering* (eds P. J. Culligan, H. H. Einstein and A. J. Whittle), pp. 1997–2004. Essen, Germany: Verlag Glückauf GmbH.

Johansson, E. & Sandeman, E. (2014). *Modelling of a deep excavation in soft clay a comparison of different calculation methods to in situ measurements.* Master's thesis, Chalmers University of Technology, Gothenburg, Sweden.

Kulhawy, F. H. & Mayne, P. W. (1990). *Manual on estimating soil properties for foundation design*, *no. EPRI-EL-6800* (prepared by Cornell University, Ithaca, NY, USA). Palo Alto, CA, USA: Electric Power Research Institute.

Langford, J., Karlsrud, K., Bengtsson, E., Hof, C. & Oscarsson, R. (2021). Comparison between predicted and measured performance of a deep excavation in soft clay in Gothenburg, Sweden. In *Geotechnical aspects of underground construction in soft ground* (eds M. Elshafie, G. Viggiani and R. Mair), pp. 83–90. Leiden, the Netherlands: CRC Press/Balkema.

Liu, G. B., Ng, C. W. & Wang, Z. W. (2005). Observed performance of a deep multistrutted excavation in Shanghai soft clays. *J. Geotech. Geoenviron. Engng* **131**, No. 8, 1004–1013.

Liu, G. B., Jiang, R. J., Ng, C. W. & Hong, Y. (2011). Deformation characteristics of a 38 m deep excavation in soft clay. *Can. Geotech. J.* **48**, No. 12, 1817–1828.

Long, M. (2001). Database for retaining wall and ground movements due to deep excavations. *J. Geotech. Geoenviron. Engng* **127**, No. 3, 203–224.

Mana, A. I. & Clough, G. W. (1981). Prediction of movements for braced cuts in clay. *J. Geotech. Engng Div.* **107**, No. 6, 759–777.

Masini, L., Gaudio, D., Rampello, S. & Romani, E. (2021). Observed performance of a deep excavation in the historical center of Rome. *J. Geotech. Geoenviron. Engng* **147**, No. 2, 05020015.

Moormann, C. (2004). Analysis of wall and ground movements due to deep excavations in soft soil based on a new worldwide database. *Soils Found.* **44**, No. 1, 87–98.

Ng, C. W. W., Hong, Y., Liu, G. B. & Liu, T. (2012). Ground deformations and soil–structure interaction of a multi-propped excavation in Shanghai soft clays. *Géotechnique* **62**, No. 10, 907–921, https://doi.org/10.1680/geot.10.P.072.

NGI (Norwegian Geotechnical Institute) (1962). *Measurements at a strutted excavation, Oslo subway, Vaterland 1*, Technical Report 7. Oslo, Norway: NGI.

Orazalin, Z. Y., Whittle, A. J. & Olsen, M. B. (2015). Three-dimensional analyses of excavation support system for the Stata Center basement on the MIT campus. *J. Geotech. Geoenviron. Engng* **141**, No. 7, 05015001, https://doi.org/10.1061/(ASCE)GT.1943-5606.0001326.

Ou, C. Y., Hsieh, P. G. & Chiou, D. C. (1993). Characteristics of ground surface settlement during excavation. *Can. Geotech. J.* **30**, No. 5, 758–767.

Peck, R. B. (1969). Deep excavation & tunnelling in soft ground: state of the art report. In *Proceedings of the 7th international conference of soil mechanics and foundation engineering*, pp. 225–281. Mexico City, Mexico: Sociedad Mexicana de Mecanica.

Powrie, W. & Batten, M. (2000). Comparison of measured and calculated temporary-prop loads at Canada Water Station. *Géotechnique* **50**, No. 2, 127–140, https://doi.org/10.1680/geot.2000.50.2.127.

Pujades, E., Vàzquez-Suñé, E., Carrera, J. & Jurado, A. (2014). Dewatering of a deep excavation undertaken in a layered soil. *Engng Geol.* **178**, 15–27.

Richards, D. J., Holmes, G. & Beadman, D. R. (1999). Measurement of temporary prop loads at Mayfair car park. *Proc. Instn Civ. Engrs Geotech. Engng* **137**, No. 3, 165–174, https://doi.org/10.1680/gt.1999.370305.

Robertson, P. K. (2009). Interpretation of cone penetration tests—a unified approach. *Can. Geotech. J.* **46**, No. 11, 1337–1355.

Robertson, P. K. (2010). Soil behaviour type from the CPT: an update. In *CPT '10: 2nd international symposium on cone penetration testing, conference proceedings* (eds P. K. Robertson and P. W. Mayne), vol. 2, pp. 575–582. Huntington Beach, CA, USA: CPT '10 Organizing Committee.

Roboski, J. F. (2004). *Three-dimensional performance and analyses of deep excavations*. PhD thesis, Northwestern University, Evanston, IL, USA.

Royston, R. (2018). *Investigation of soil–structure interaction for large diameter caissons*. Doctoral thesis, University of Oxford, Oxford, UK.

St John, H. D., Higgins, K. G., Potts, D. M. & Jardine, R. J. (1992). Prediction and performance of ground response due to construction of a deep basement at 60 Victoria embankment. In *Predictive soil mechanics: proceedings of the Wroth memorial symposium held at St Catherine's College, Oxford, 27–29 July 1992* (eds G. T. Houlsby and A. N. Schofield), pp. 581–608. London, UK: Thomas Telford Publishing.

Swatek, E. P., Asrow, S. P. & Seitz, A. M. (1972). Performance of bracing for deep Chicago excavation. In *Proceedings of the specialty conference on performance of earth and earth-supported structures*, vol. 1, part 2, pp. 1303–1322. New York, NY, USA: American Society of Civil Engineers.

Tan, Y. & Wei, B. (2012). Observed behaviors of a long and deep excavation constructed by cut-and-cover technique in Shanghai soft clay. *J. Geotech. Geoenviron. Engng* **138**, No. 1, 69–88.

Tan, Y., Lu, Y. & Wang, D. (2018). Deep excavation of the Gate of the Orient in Suzhou stiff clay: composite earth-retaining systems and dewatering plans. *J. Geotech. Geoenviron. Engng* **144**, No. 3, 05017009.

Tornborg, J., Karlsson, M., Kullingsjö, A. & Karstunen, M. (2021). Experience from short- and long-term performance of deep excavations in soft sensitive clays. *IOP Conf. Ser.: Earth Environ. Sci.* **710**, 012053.

Tschebotarioff, G. (1973). Foundations, retaining and earth structures – the art of design and construction and its scientific bases in soil mechanics. London, UK: McGraw-Hill Education.

Twine, D. & Roscoe, H. (1997). *Temporary propping of deep excavations – guidance on design*. London, UK: Construction Industry Research and Information Association.

Wang, J. H., Xu, Z. H. & Wang, W. D. (2010). Wall and ground movements due to deep excavations in Shanghai soft soils. *J. Geotech. Geoenviron. Engng* **136**, No. 7, 985–994.

Wu, S. H., Ching, J. & Ou, C. Y. (2013). Predicting wall displacements for excavations with cross walls in soft clay. *J. Geotech. Geoenviron. Engng* **139**, No. 6, 914–927.